

# **Giant second harmonic generation in supertwisted WS<sub>2</sub> spirals grown in step edge particle induced non-Euclidean surfaces**

Tong Tong<sup>1,2,‡</sup>, Ruijie Chen<sup>1,‡</sup>, Yuxuan Ke<sup>3</sup>, Qian Wang<sup>1</sup>, Xinchao Wang<sup>1</sup>, Qinjun Sun<sup>2</sup>, Jie Chen<sup>1</sup>, Zhiyuan Gu<sup>1</sup>, Ying Yu<sup>1</sup>, Hongyan Wei<sup>1</sup>, Yuying Hao<sup>1</sup>, Xiaopeng Fan<sup>1,\*</sup>, and Qing Zhang<sup>3,\*</sup>

<sup>1</sup>College of Electronic Information and Optical Engineering, Taiyuan University of Technology, Taiyuan 030024, China.

<sup>2</sup>College of Physics, Taiyuan University of Technology, Taiyuan 030024, China.

<sup>3</sup>School of Materials Science and Engineering, Peking University, Beijing 100871, China

Correspondence: Qing Zhang (q\_zhang@pku.edu.cn), Xiaopeng Fan (xiaopengfan@tyut.edu.cn)

## **Abstract**

In moiré crystals resulting from the stacking of twisted two-dimensional (2D) layered materials, a subtle adjustment in the twist angle surprisingly gives rise to a wide range of correlated optical and electrical properties. Herein, we report the synthesis of supertwisted WS<sub>2</sub> spirals and the observation of giant second harmonic generation (SHG) in these spirals. Supertwisted WS<sub>2</sub> spirals featuring different twist angles are synthesized on a Euclidean or step-edge particle-induced non-Euclidean surface using a carefully designed water-assisted chemical vapor deposition deposition. We observed an oscillatory dependence of SHG intensity on layer number, attributed to atomically phase-matched nonlinear dipoles within layers of supertwisted spiral crystals where inversion symmetry is restored. Through an investigation into the twist angle evolution of SHG intensity, we discovered that the stacking model between layers plays a crucial role in determining the nonlinearity, and the SHG signals in supertwisted spirals exhibit enhancements by a factor of 2 to 136 when compared with the SHG of the single-layer structure. These findings provide an efficient method for the rational growth of 2D twisted structures and the implementation of twist angle adjustable endowing them great potential for exploring strong coupling correlation physics and applications in the field of twistronics.

**Keywords:** WS<sub>2</sub>, supertwisted spiral, second harmonic generation, twist angle

## Introduction

The emerging twisted van der Waals (vdW) structures offer a variety of attractive building blocks for the study of various extraordinary physical phenomena<sup>1-5</sup>. For example, the twisted vdW structures with multiple vertically stacked layers create periodic moiré lattices due to lattice mismatches or twist angles<sup>6</sup>. The twist angle determines the dynamics within the mini-Brillouin zone<sup>7-9</sup>, which induces strongly correlated quantum phenomena ranging from moiré excitons<sup>10-13</sup>, moiré phonons<sup>14,15</sup> and an enhanced photoresponse<sup>16,17</sup> in optics to superconductivity<sup>1</sup>, as well as ferromagnetism<sup>18</sup> and fractional quantum Hall effects<sup>19,20</sup> in electronics. In particular, the twisted vdW structures feature an almost arbitrary geometry that is consistent with the crystallographic symmetry groups of the sublattices, and therefore offer a new avenue for quantum manipulation of quasiparticles in quantum optics. Recently, the supertwisted spiral moiré lattices in supertwisted WS<sub>2</sub>/WSe<sub>2</sub> spirals were resolved, enabling special twist angle-dependent morphologies<sup>21</sup>. These angle-dependent twisted vdW structures hold promise for exploring the strong coupling correlation physics of twistrionics<sup>22,23</sup>, including optics, electronics, acoustics, condensed matter and quantum physics<sup>24</sup>. However, the relationship between the second harmonic generation (SHG) effect of 2D twisted vdW structures and the twist angle of the layers needs further investigation, particularly for 2D supertwisted spirals with more than two layers.

Here we investigate the evolution of the SHG effect based on supertwisted WS<sub>2</sub> spirals obtained on a Euclidean or step edge particle induced non-Euclidean surface.

We present the experimental realization of supertwisted spiral with continuous twist angles and modified symmetry. The supertwisted WS<sub>2</sub> lattices are obtained by screw-dislocation-driven (SDD) growth and have a tunable twist angle. Depending on the twist angle, spiral structures with a different periodic structure enable inversion symmetry breaking and thus a giant SHG effect. Overall, these findings pave a new path to manipulate the structural symmetry in vdW layered materials for further studies in strongly correlated physics and twistrionics.

## **Results and Discussion**

### **One-step growth of step edge particles induced supertwisted WS<sub>2</sub> spirals**

Van der Waals materials are materials with strong in-plane covalent bonding and weak interlayer interactions. The 2D nature of these materials makes them easy to bend and less sensitive to the epitaxial relationship of the underlying substrate. Those properties make it easier for van der Waals materials growth be influenced by the geometry of the growth substrate. We achieve the growth of supertwisted WS<sub>2</sub> spirals via a water vapor-assisted chemical vapor deposition (CVD) process (Fig. S1). Briefly, WS<sub>2</sub> powder was filled in a quartz boat and then placed in the heating center of the furnace, and a silicon substrate with 280 nm SiO<sub>2</sub> was placed downstream for material deposition (See Materials and Methods for growth details). The key step in the growth of supertwisted spiral WS<sub>2</sub> is the introduction of deionized water. In particular, 0.05–0.1 ml deionized water was dropped onto the edge of another quartz boat. This keeps the water droplets in an elliptical shape and prevents them from

evaporation before heating. The boat with water was then placed 20–25 cm upstream from the WS<sub>2</sub> powder (outside the insulation of the tube furnace to prevent the deionized water from evaporating too quickly when heated). In previous work, we have demonstrated that the water here can serve as a transport agent to promote the dissociation and volatilization of the WS<sub>2</sub> precursor<sup>25,26</sup> by forming volatile WO<sub>x</sub>(OH)<sub>y</sub> gas species and H<sub>2</sub>S gas. Those gas species lead to increased vapor pressure and, accordingly, increased nucleation. The volatile WO<sub>x</sub>(OH)<sub>y</sub> can also decompose and form WO<sub>x</sub> particles, which tends to form on the edge of the growing WS<sub>2</sub>. Those WO<sub>x</sub> particles can act as the nucleation site to a screw dislocation (red dotted circle in Fig. 1a and inset model in Fig. 1c). As growth proceeds, the continuously supplied vapor species from the precursor enable additional nucleation and growth on the newly formed ribbons, ultimately forming the supertwisted WS<sub>2</sub> spirals (Fig. S2a-h).

Fig. 1a and 1b are the optical and atomic force microscopy (AFM) images of a left-handed supertwisted WS<sub>2</sub> spirals, which is located on top of a WO<sub>x</sub> particle formed on the step edge of WS<sub>2</sub> nanoribbon. AFM shows the height of the black band underneath of the WS<sub>2</sub> spiral is about 1.4 nm (Fig. 1c), which corresponds to the thickness of two WS<sub>2</sub> monolayer. It indicates that a bilayer WS<sub>2</sub> ribbon is underneath the WS<sub>2</sub> spiral. During the SDD growth process, the WO<sub>x</sub> particles are formed on the edge of the nanoribbons, as shown by the red dashed circle in Figure 1a. The formation of these particles provides a non-Euclidean substrate for the growth of the spiral structures (inset in Fig. 1c). Fig. 1d and 1e are the optical and AFM images of a

right-handed supertwisted  $\text{WS}_2$  spiral. The twist angle was defined by the angle between each layer (Fig. 1f). And the height of each layer of the  $\text{WS}_2$  spiral is about 0.7 nm (Fig. 1g). Fig. S2f-h provides more details of the left/right-handed supertwisted  $\text{WS}_2$  spirals. Optical microscope allows us to quickly and roughly identify the spirals with different twist angles. Under an optical microscope, the spirals with near zero angles have triangular shapes (Fig. S3a, b), while the spirals with large twist angles show a circular shape (Fig. S2f-h). This is a good indication of the supertwisted structures. Fig. 1h show the structural model of the right-handed supertwisted  $\text{WS}_2$  spiral with different twist angle.

The shape of these supertwisted spirals can be explained by the geometric mismatch between lattice and the underlying substrate<sup>21</sup>. Because 2D materials are easy to bend and less sensitive to the epitaxial relationship of the underlying substrate, they trend to follow the geometry of the underlying substrate<sup>27-29</sup> despite inducing strain. In typical CVD of  $\text{WS}_2$ <sup>25,26</sup>, the  $\text{WS}_2$  spirals are grown on a flat  $\text{SiO}_2/\text{Si}$  substrate, which is a Euclidean surface with an angular period of  $2\pi$ . Therefore, the  $\text{WS}_2$  spiral grows into a triangle with the edges of different layers aligned in parallel (Fig. 2a-c)<sup>30,31</sup>. However, when the screw dislocation locates on a protrusion which is a non-Euclidean surface, the SDD growth would result in a very different morphology called supertwisted spirals (Fig. 2d-k)<sup>21</sup>. There are two different cases when growing supertwisted spirals on a conical surface: (i) Fig. 2d shows the angular period of the substrate is  $2\pi-\alpha$  ( $\alpha>0$ ), which corresponds to a crystal grows at the apex of a cone. Thus, each complete lattice period ( $2\pi$ ), the lattice carries an

excess angle of  $\alpha$  going into the next cycle (Fig. 2e). For a right-handed spiral (counterclockwise from bottom to top), this causes the triangular edges in each layer rotated counterclockwise by an angle of  $\alpha$  with respect to the bottom layer, resulting in a right-handed supertwisted spirals, as shown in Fig. 2f. In this case, the center of the dislocation coincides with the top center of a protruding cone, as shown in Fig. 2g. (ii) Fig. 2h indicates that the angular period of the substrate surface is  $2\pi+\alpha$  ( $\alpha>0$ ), which corresponds to a warped "hyperbolic cone" surface. Since the angular period of the surface is larger than the lattice period, one lattice period is unable to cover the surface of the substrate (Fig. 2i). As a result, an angle of  $\alpha$  needs to be "borrowed" from the next lattice period. This causes the triangular edges in each layer rotated clockwise by an angle of  $\alpha$  with respect to the previous layer, resulting in left-handed twisted spirals, as shown in Fig. 2j. In this case, the center of the dislocation coincides with the edge of the protruding cone (Fig. 2k).

### **Twist angle-dependent nonlinear optical effects**

We examined the nonlinear optical properties of these atomically WS<sub>2</sub> spirals. The relationship between the twist angle-dependent SHG of WS<sub>2</sub> spirals and the number of layers were investigated using a reflection mode. The thickness-dependent SHG intensity of supertwisted WS<sub>2</sub> spirals shows that all regions have a remarkable SHG signal (Fig. 3). Fig. 3a-c show the SHG from a normal triangular WS<sub>2</sub> spiral ( $\approx 0^\circ$  twist angle). Its SHG intensity increases with increasing number of layers, and the maximum SHG signal in 30L is enhanced over 136 times compared to WS<sub>2</sub> monolayer (Table 1 and Fig. S5a, b). This is because this WS<sub>2</sub> spiral has the 3R phase

structure with broken inversion symmetry<sup>30,34</sup>. As the layer numbers increase, the SHG intensity increases rapidly, giant SHG was therefore observed in these triangular WS<sub>2</sub> spirals. However, when a WS<sub>2</sub> spiral is supertwisted (Fig. 3d-l), there's an oscillating SHG intensity with increasing number of layers and twist angles. Yet, the SHG intensity of the supertwisted spirals is always higher than that of monolayer WS<sub>2</sub> (Table 1). For example, in the supertwisted WS<sub>2</sub> spiral with a twist angle of 13° (Fig. 3d-f), the SHG intensity in 1L–5L gradually increases from 4 times to 92 times as layer number increases compared to monolayer WS<sub>2</sub>, just like the WS<sub>2</sub> spiral with 3R phase. However, the SHG intensity decreased rapidly in 6L–7L. The SHG intensity of the supertwisted WS<sub>2</sub> spiral with a twist angle of 16° (Fig. 3g-i) and 20° (Fig. 3j-l) also show the same oscillating behavior. Another interesting observation is that the onset of SHG decline region changes from 6L to 5L to 4L as the twist angle increases from 13° to 16° to 20°, respectively. Despite being similar thickness, as the twist angle increase, the SHG signal reaches the strongest point faster and start to decline, the interference effect can be ignored compared to structural symmetry and the oscillation period is obviously reduced with the increase of the number of layers. Overall, depending on the twist angles and layers, the SHG signal can be amplified 12–136 times for the  $\approx 0^\circ$  spiral<sup>32,33</sup>, 4–92 times for the 13° spiral, 2–45 times for the 16° spirals, and 4–41 times for the 20° spiral, respectively (Table 1). Both the maximum and minimum enhancement factors decrease with increasing twist angles.

To explain the oscillating SHG behavior, we further analyzed the effect of inversion symmetry on the SHG of the supertwisted WS<sub>2</sub> spirals, as show in Fig 4.

Here we use a stacked WS<sub>2</sub> model to represent the local structural symmetry of supertwisted spiral structures. Fig. 4a and 4b corresponds to the top view and side view of multilayer WS<sub>2</sub> structures, respectively. Given  $\alpha=20^\circ$ , the twist angle between the first two layers is  $20^\circ$  (Fig. 4b) and between Layer 1 and Layer 3 is  $40^\circ$  (Fig. 4c). They all exhibit broken inversion symmetry, resulting in increased SHG intensity with layer numbers. In contrast, as the twisted layer increases toward the fourth layer, the twist angle relative to the first layer is  $60^\circ$  (the last image of Fig. 4a, b). The inversion symmetry between the first layer and the fourth layer is then restored, resulting a reduced overall SHG. However, since the fourth layer maintains a twist angle of  $40^\circ$  and  $20^\circ$  relative to the second and third layers, respectively, the SHG intensity of the fourth layer would not decrease to zero (Fig. 31). Fig 4c showed the corresponded side view when stacked 7 layers, and it can be seen that each interval of  $60^\circ$  corresponds to the bilayer reversal symmetry recovery. In addition, Hsu *et al.* found that twist angles of  $2^\circ$ ,  $16^\circ$ ,  $30^\circ$ , and  $37^\circ$  all resulted in an enhancement of the SHG intensity in the stacked region with respect to monolayer MoS<sub>2</sub><sup>35,36</sup>. However, when the twist angle is  $54^\circ$ , the SHG intensity is smaller than that of monolayer MoS<sub>2</sub>, suggesting that the SHG of twisted bilayer MoS<sub>2</sub> is a coherent superposition of SHG fields from individual layers<sup>37</sup>. The SHG of a 2H phase hexagonal WS<sub>2</sub> spiral was also examined, and the results are shown in Fig. S5 c-f. The angle between two screw dislocations of the hexagonal spiral WS<sub>2</sub> is  $60^\circ$  (Fig. S5e), resulting in inversion symmetry exist in hexagonal spiral<sup>38</sup>. Fig S5f confirms that the SHG signal disappears in even layers. In short, for supertwisted WS<sub>2</sub> spiral, if the cumulative twist angle is within  $60^\circ$ , the

whole inversion symmetry is broken, the nonlinear signal is gradually enhanced with the increase of the number of layers; when the cumulative twist angle is greater than 60 degrees, the inversion symmetry is restored between the local specific two layers. These specific two layers may suffer from the SHG quenching effect, the nonlinear signal is gradually weakened with the increase of the number of layers and then a periodic oscillation occurs. At the same time, the oscillation rate of the nonlinear signal is related to the twist angle, the smaller the twist angle, the slower the oscillation rate, and the vice versa. Therefore, the SHG intensity mainly depends on the inversion symmetry broken of the crystal structure<sup>39-41</sup>.

## **Conclusions**

In summary, we found that the atomically supertwisted WS<sub>2</sub> spirals with different twist angles can be grown on Euclidean or non-Euclidean surfaces using a one-step water vapor-assisted chemical vapor deposition. The SHG signals in these spirals can be amplified up to 2–136 times depending on their twist angles. The spectroscopic measurements in these spirals suggest a continuous and subtle evolution of atomic configuration. The inversion symmetry is modified as the twist angle changes, leading to a faster increase in SHG intensity of the twisted spirals with smaller twist angles. In a certain range of small twist angles ( $\approx 0^\circ$ ), a maximum SHG enhancement was observed with increasing layer number, which originates from the broken inversion symmetry. Our work implies that the supertwisted WS<sub>2</sub> spirals could provide an attractive platform for the study of light-matter interactions.

## **Materials and Methods**

### **Water vapor-assisted chemical vapor deposition growth of WS<sub>2</sub> spirals**

The atomically supertwisted WS<sub>2</sub> spirals were synthesized by water vapor-assisted chemical vapor deposition on a silicon wafer covered with 280 nm SiO<sub>2</sub>. WS<sub>2</sub> powder in a quartz boat was placed at the heating center of a quartz tube in the CVD setup. 0.5–1 ml deionized water was placed upstream outside the heating zone as the water vapor source. The substrates were placed about 6–8 cm downstream (700–800 °C) of the quartz tube. High purity argon with flow rate of 80 sccm was introduced into the CVD system for 40 min to discharge the oxygen inside the tube before heating. Then, the furnace was heated to 1150 °C in 35–40 min with an argon flow of 80 sccm and maintained at this temperature for 15–25 min for spiral WS<sub>2</sub> growth.

### **Material characterizations**

The morphology of spiral WS<sub>2</sub> was characterized by optical microscopy (Zeiss Axio Imager A1) and atomic force microscopy (AFM Bruker Multimode 8-HR, AFM probe: Scanasyst-AIR with  $f_0=70$  kHz,  $k=0.4$  N/m,  $T=650$  nm,  $L=115$   $\mu$ m and  $W=25$   $\mu$ m.).

SHG measurements were performed using a custom-built confocal microscope in reflection geometry and a Ti: Sapphire laser (Chameleon Ultra) at 800 nm. The laser was vertically incident on the spiral WS<sub>2</sub>. A 100 $\times$  microscope objective (Olympus, NA = 0.9) was used to collect reflection light. The SHG signals through a short-pass filter (Thorlabs, cut-off wavelength: 532 nm) were recorded by a charge-coupled

device (CCD). The size of the laser spot was 2  $\mu\text{m}$ , and power was 84  $\text{mW}/\text{cm}^2$ .

## References

1. Cao, Y. et al. Unconventional superconductivity in magic-angle graphene superlattices. *Nature* **556**, 43-50 (2018).
2. Ye, T. et al. Nonvolatile electrical switching of optical and valleytronic properties of interlayer excitons. *Light Sci. Appl.* **11**, 23 (2022).
3. Yang, J. et al. Optical tuning of exciton and trion emissions in monolayer phosphorene. *Light Sci. Appl.* **4**, e312 (2015).
4. Naik, M. H. et al. Intralayer charge-transfer moiré excitons in van der Waals superlattices. *Nature* **609**, 52–57 (2022).
5. Wang, H. F. et al. Intrinsic superflat bands in general twisted bilayer systems. *Light Sci. Appl.* **11**, 159 (2022).
6. Sharpe, A. L. et al. Emergent ferromagnetism near three-quarters filling in twisted bilayer graphene. *Science* **365**, 605–608 (2019).
7. Chen, G. R. et al. Tunable correlated chern insulator and ferromagnetism in a moiré superlattice. *Nature* **579**, 56–61 (2020).
8. S Zheng. et al. Localization-enhanced moiré exciton in twisted transition metal dichalcogenide heterotrilayer superlattices. *Light Sci Appl* **12**, 117 (2023).
9. Wang, L. et al. Correlated electronic phases in twisted bilayer transition metal dichalcogenides. *Nat. Mater.* **19**, 861–866 (2020).
10. Jin, C. H. et al. Observation of moiré excitons in  $WSe_2/WS_2$  heterostructure superlattices. *Nature* **567**, 76–80 (2019).
11. Seyler, K. L. et al. Signatures of moiré-trapped valley excitons in  $MoSe_2/WSe_2$  heterobilayers. *Nature* **567**, 66–70 (2019).
12. Tran, K. et al. Evidence for moiré excitons in van der Waals heterostructures. *Nature* **567**, 71–75 (2019).
13. Alexeev, E. M. et al. Resonantly hybridized excitons in moiré superlattices in van der Waals heterostructures. *Nature* **567**, 81–86 (2019).
14. Quan, J. M. et al. Phonon renormalization in reconstructed  $MoS_2$  moiré superlattices. *Nat. Mater.* **20**, 1100–1105 (2021).

15. Kim, J. et al. Anomalous optical excitations from arrays of whirlpooled lattice distortions in moiré superlattices. *Nat. Mater.* **21**, 890–895 (2022).
16. Sunku, S. S. et al. Hyperbolic enhancement of photocurrent patterns in minimally twisted bilayer graphene. *Nat. Commun.* **12**,1641 (2021).
17. Hesp, N. C. H. et al. Nano-imaging photoresponse in a moiré unit cell of minimally twisted bilayer graphene. *Nat. Commun.* **12**,1640 (2021).
18. Hunt, B. et al. Massive Dirac fermions and Hofstadter butterfly in a van der Waals heterostructure. *Science* **340**, 1427–1430 (2013).
19. Ponomarenko, L. A. et al. Cloning of Dirac fermions in graphene superlattices. *Nature* **497**, 594–597 (2013).
20. Dean, C. R. et al. Hofstadter’s butterfly and the fractal quantum Hall effect in moiré superlattices. *Nature* **497**, 598–602 (2013).
21. Zhao, Y. Z. et al. Supertwisted Spirals of Layered Materials Enabled by Growth on Non-Euclidean Surfaces. *Science* **370**, 442–445 (2021).
22. Tan, Q. H. et al. Layer-dependent correlated phases in WSe<sub>2</sub>/MoS<sub>2</sub> moiré superlattice. *Nat. Mater.* **22**, 605–611 (2023).
23. Miao, S. N. et al. Strong interaction between interlayer excitons and correlated electrons in WSe<sub>2</sub>/WS<sub>2</sub> moiré superlattice. *Nat. Commun.* **12**, 3608 (2021).
24. Lamas-Linares, A., Howell, J. C. & Bouwmeester, D. Stimulated emission of polarization-entangled photons. *Nature* **412**, 887–890 (2001).
25. Meng, F. et al. Screw Dislocation Driven Growth of Nanomaterials. *Acc. Chem. Res.* **46**, 1616–1626 (2013).
26. Zhao, Y. Z. et al. Controllable Water Vapor Assisted Chemical Vapor Transport Synthesis of WS<sub>2</sub>–MoS<sub>2</sub> Heterostructure. *ACS Materials Lett.* **2**, 42–48(2020).
27. Wei, N. et al. Curvature geometry in 2D materials, *Natl. Sci. Rev.*, 10, nwad145 (2023).
28. Zeng, M., Liu, J., Zhou, L. et al. Bandgap tuning of two-dimensional materials by sphere diameter engineering. *Nat. Mater.* **19**, 528–533 (2020).
29. Kai Wang et al. Strain tolerance of two-dimensional crystal growth on curved surfaces. *Sci. Adv.* **5**, eaav4028 (2019).

30. Fan, X. P. et al. Controllable Growth and Formation Mechanisms of Dislocated WS<sub>2</sub> Spirals. *Nano Lett.* **18**, 3885-3892 (2018).
31. Shearer, M. J. et al. Complex and Noncentrosymmetric Stacking of Layered Metal Dichalcogenide Materials Created by Screw Dislocations. *J. Am. Chem. Soc.* **139**, 3496-3504 (2017).
32. Fan, X. P. et al. Broken Symmetry Induced Strong Nonlinear Optical Effects in Spiral WS<sub>2</sub> Nanosheets. *ACS Nano.* **11**, 4892-4898 (2017).
33. Peng, J. B. et al. Spatially Dependent Electronic Structures and Excitons in a Marginally Twisted moiré Superlattice of Spiral WS<sub>2</sub>. *ACS Nano* **12**, 21600–21608(2022).
34. Dong, Y. et al. Giant bulk piezophotovoltaic effect in 3R-MoS<sub>2</sub>. *Nat. Nanotechnol.* **18**, 36–41 (2023).
35. Jiang, H. J. et al. Inversion symmetry broken in 2H phase vanadium-doped molybdenum disulfide. *Nanoscale.* **13**, 18103-18111 (2021).
36. Hsu, W-T. et al. Second Harmonic Generation from Artificially Stacked Transition Metal Dichalcogenide Twisted Bilayers. *ACS Nano.* **8**, 2951-2958 (2014).
37. Ye, K. et al. Controllable growth of multilayered XSe<sub>2</sub> (X = W and Mo) for nonlinear optical and optoelectronic applications. *2D Mater.* **9**, 015012 (2022).
38. Ci, P. H. et al. Breaking Rotational Symmetry in Supertwisted WS<sub>2</sub> Spirals via moiré Magnification of Intrinsic Heterostrain. *Nano Lett.* **22**, 9027-9035 (2022).
39. Fan, X. P. et al. Mechanism of Extreme Optical Nonlinearities in Spiral WS<sub>2</sub> above the Bandgap. *Nano Lett.* **20**, 2667-2673 (2020).
40. Zhao, M. et al. Atomically phase-matched second-harmonic generation in a 2D crystal. *Light. Sci. Appl.* **5**, e16131 (2016).
41. Wang, X. et al. Water-Assisted Growth of Twisted 3R-Stacked MoSe<sub>2</sub> Spirals and Its Dramatically Enhanced Second Harmonic Generations. *Small* **19**, 2301828 (2023).

## **Acknowledgements**

The authors express their gratitude to various organizations for their support in this research, including the National Natural Science Foundation of China (Grant No. 52273252, 11804408, 62105232, 52072006, U23A2076), the Fundamental Research Program of Shanxi Province (Grant No. 20210302124027, 20210302124169, 202203021221080).

## **Author contributions**

The project was designed and managed by XPF and QZ. The samples were synthesized and characterized by TT. AFM measurements were provided by TT, and RJC. SHG measurements were obtained by TT, and YY. Interpretation of data was provided by XPF, QZ, QJS, JC, ZYG, HYW and YYH. XPF, QZ revised the manuscript. All authors reviewed and contributed the revision of the manuscript.

†TT, and RJC contributed equally to this work.

## **Conflict of interest**

The authors declare no competing interest.

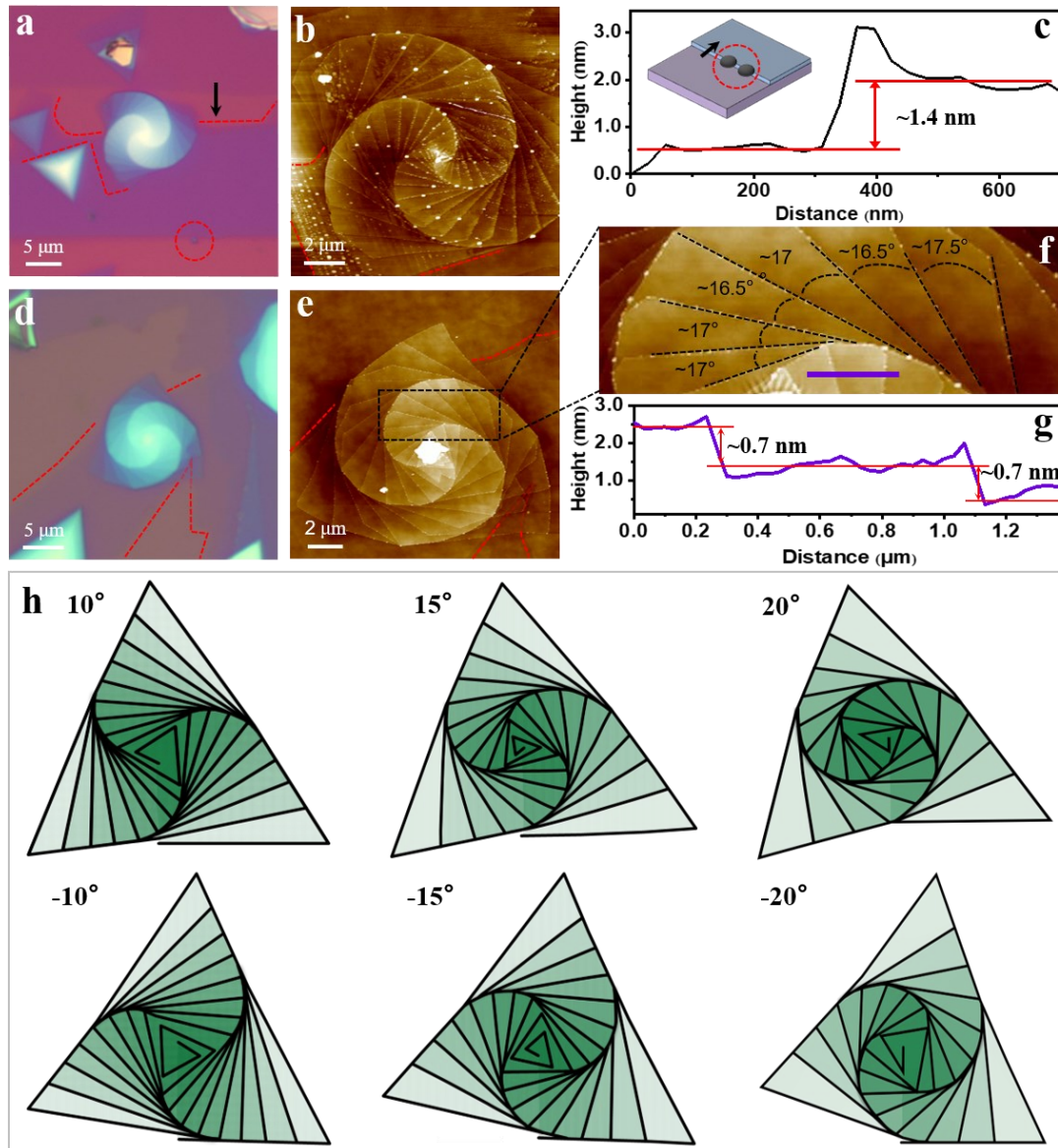


**Figure 1. Atomically Supertwisted WS<sub>2</sub> spiral with different twist angles. a, b** Optical and AFM image of the left-handed supertwisted WS<sub>2</sub> spiral. **c** Line profile marked with a black line in (b) showing that the height of the ribbon was about 1.4 nm. This suggested that twisted spiral WS<sub>2</sub> grows on the ribbon. **d, e** Optical and AFM image of the right-handed supertwisted WS<sub>2</sub>. **f** Line profile marked with a purple line in upper showing that the height of each layer was about 0.7 nm. **g** the twist angle was defined by the angle between each layer. **h** Structural model of the right-handed supertwisted WS<sub>2</sub> spiral with different twist angles.

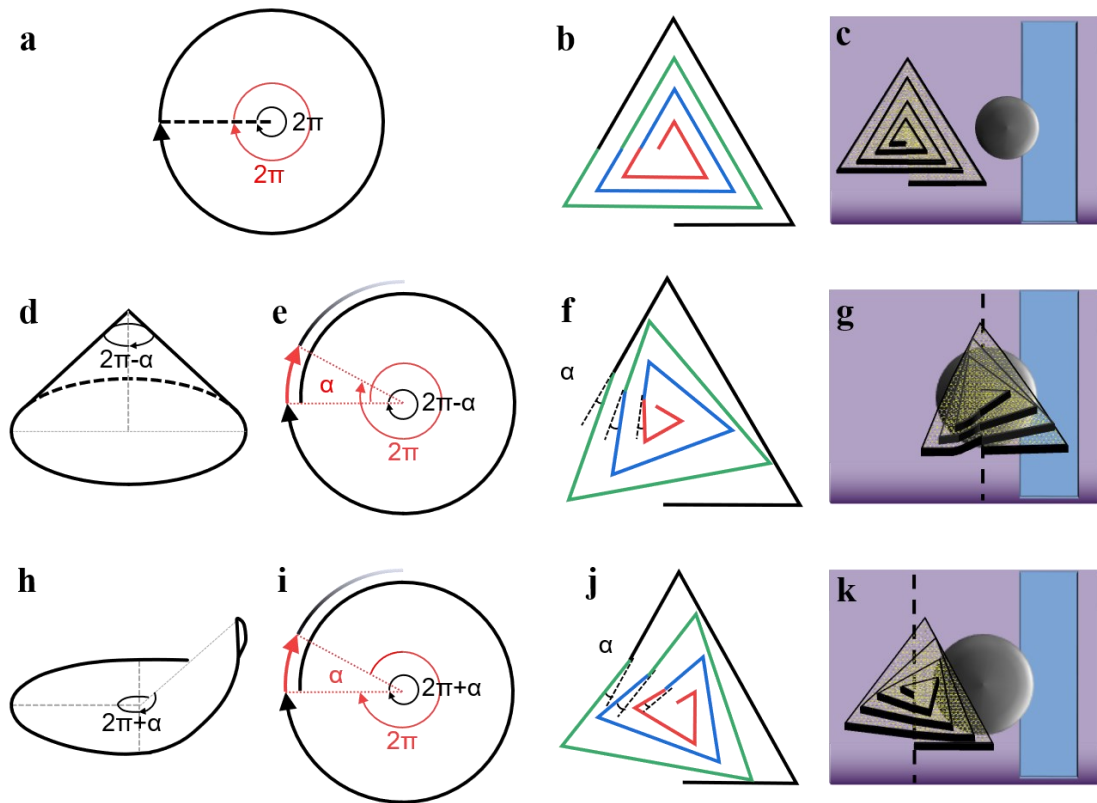


**Figure 2. Formation mechanisms of supertwisted spiral  $\text{MX}_2$  on different surfaces.** **a**,  $2\pi$  angular period of lattice and substrate with a Euclidean surface. The black circular arrow indicates sample angular period, the red arrow indicates  $2\pi$  angular period. **b**, Schematic structure of a right-handed  $\text{MX}_2$  spiral. Each layer with  $2\pi$  angular period is marked with different color. **c**, Schematic growth model of spiral  $\text{MX}_2$ . The purple region represents the  $\text{SiO}_2/\text{Si}$  wafer, the blue region represents a  $\text{WS}_2$  nanoribbon, and the gray circle represents a  $\text{WO}_x$  nanoparticle formed on the edge of the  $\text{WS}_2$  nanoribbon. **d**, **e**  $2\pi-\alpha$  angular period on a non-Euclidean cone surface, the conical surface is formed due to clipping an angle of  $\alpha$ . **f**, Schematic crystal structure of the left-hand twisted spiral  $\text{MX}_2$ , with the dislocation center at the apex of the cone (**g**). **h**, **i**  $2\pi+\alpha$  angular period on a non-Euclidean “hyperbolic cone” surface, the surface is formed due to “borrowing”  $\alpha$  degree from the next period. **j** Schematic crystal structure of the left-hand twisted spiral  $\text{MX}_2$ , with the dislocation center at the edge of the cone (**k**)

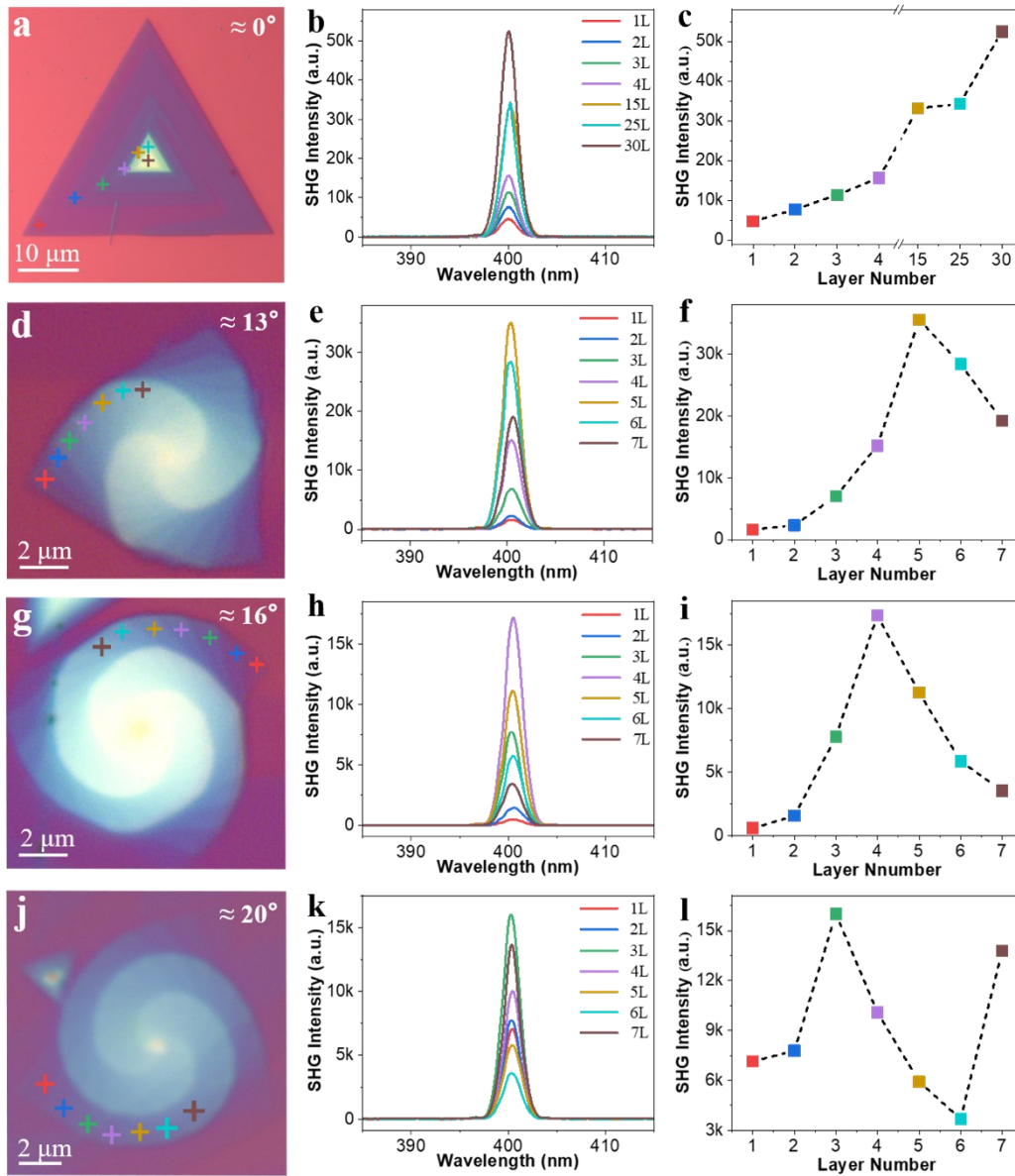


**Figure 3. Angle-dependent SHG of twist spiral WS<sub>2</sub>.** **a** Optical image of the twisted spiral WS<sub>2</sub> and layer-dependent SHG. **(b, c)** **d-l** Optical image of the supertwisted WS<sub>2</sub> spiral with  $\alpha \approx 13^\circ$  (**d**),  $\alpha \approx 16^\circ$  (**g**) and  $\alpha \approx 20^\circ$  (**j**), and their layer-dependent SHG (**e, f**), (**h, i**), (**k, l**), respectively. The colored crosses in these figures show the region where SHG signals are collected. The larger the region number, the thicker the layer.

**Table 1.** The SHG absolute intensity and SHG intensity rate of monolayer WS<sub>2</sub> and supertwisted WS<sub>2</sub> spirals with twist angle at  $\approx 0^\circ$ ,  $13^\circ$ ,  $16^\circ$  and  $20^\circ$

SHG Intensity	Monolayer	Supertwisted WS <sub>2</sub> Spirals			
	WS <sub>2</sub>	$\approx 0^\circ$	$13^\circ$	$16^\circ$	$20^\circ$
Absolute Intensity (a.u.)		Max.-Min.	Max.-Min.	Max.-Min.	Max.-Min.
	386	52458-472	35551-162	17356-552	16013-367
		0	4		7
Intensity Ratio ( $I_{\text{Spirals}}/I_{\text{Monolayer}}$ )		Max.-Min.	Max.-Min.	Max.-Min.	Max.-Min.
		136-12	92-4	45-2	41-10

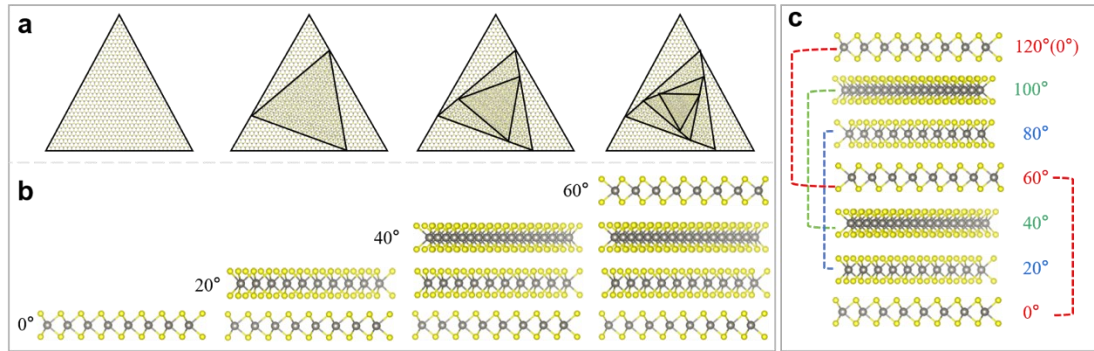


**Figure 4. Inversion symmetry of supertwisted WS<sub>2</sub> spiral.** Schematic drawing of the stacked bilayer WS<sub>2</sub> with  $\alpha=0^\circ$  (a),  $\alpha=20^\circ$  (b), the stacked tri-layer (c) and four-layer (d) WS<sub>2</sub> with twist angle  $\alpha=20^\circ$ . e Correspond to the side view of (a)-(d), respectively. f the side view of stacked 7 layers with  $20^\circ$  twist angle, layers of the same color differ by  $60^\circ$ , with a new restoration of inverted symmetry.